

1      **Lateral migration patterns toward or away from injection wells for earthquake  
2      clusters in Oklahoma**

3      **J. A. López-Comino<sup>1,2,3,4</sup>, M. Galis<sup>5,6</sup>, P. M. Mai<sup>1</sup>, X. Chen<sup>7</sup>, D. Stich<sup>2,3</sup>**

4      <sup>1</sup> KAUST, King Abdullah University of Science and Technology, Thuwal (Saudi Arabia).

5      <sup>2</sup> Instituto Andaluz de Geofísica, Universidad de Granada, Granada, Spain.

6      <sup>3</sup> Departamento de Física Teórica y del Cosmos, Universidad de Granada, Granada, Spain.

7      <sup>4</sup> Institute of Earth and Environmental Sciences, University of Potsdam, D-14476 Potsdam-  
8      Golm, Germany

9      <sup>5</sup> Faculty of Mathematics, Physics and Informatics, Comenius University in Bratislava, Slovakia

10     <sup>6</sup> Earth Science Institute, Slovak Academy of Sciences, Bratislava, Slovakia

11     <sup>7</sup> School of Geosciences, The University of Oklahoma, Norman, OK, USA

12     Corresponding author: José Ángel López-Comino (jose.lopezcomino@kaust.edu.sa)

13     **Key Points (140 characters)**

- 14     • We introduce new parameters to analyze lateral seismicity migration patterns toward or  
15     away from multiple associated fluid-injection wells
- 16     • Cluster-well distance appears as the main factor in migration behavior in comparison  
17     with injected volumes or equivalent magnitudes
- 18     • Migration away from injection wells is found for distances shorter than 5-13 km,  
19     migration toward the wells at larger distances

21     **Abstract (150 words)**

22     Exploring the connections between injection wells and seismic migration patterns is key to  
23     understanding processes controlling growth of fluid-injection induced seismicity. Numerous  
24     seismic clusters in Oklahoma have been associated with wastewater disposal operations,  
25     providing a unique opportunity to investigate migration directions of each cluster with respect to  
26     the injection-well locations. We introduce new directivity migration parameters to identify and  
27     quantify lateral migration toward or away from the injection wells. We take into account  
28     cumulative volume and injection rate from multiple injection wells. Our results suggest a  
29     relationship between migration patterns and the cluster-well distances, and unclear relationship  
30     with injected volume and equivalent magnitudes. Migration away from injection wells is found  
31     for distances shorter than 5-13 km, while an opposite migration towards the wells is observed for  
32     larger distances, suggesting an increasing influence of poroelastic stress changes. This finding is  
33     more stable when considering cumulative injected volume instead of injection rate.

## 36 Plain Language Summary

37 Oklahoma seismicity has been linked to wastewater injection and provides one of the most  
38 important datasets to explore connections between injection wells and induced seismicity. This  
39 induced seismicity can be associated in different groups (or clusters) that reveal specific  
40 spatiotemporal relationships from which preferred spatial migration directions can be identified.  
41 We analyzed seismic migration directions of these clusters with the aim of understanding the  
42 growth of the rupture process and its location with respect to the closest injection wells. We  
43 introduce new techniques and parameters to quantify lateral migration patterns toward or away  
44 from injection-well locations. Different variables such as the cluster-well distance, injected  
45 volumes and magnitudes are considered to assess their influence in these migration behaviors.  
46 We identify the main pattern depending on the cluster-well distances. At shorter distances (up to  
47 13 km), we observe dominantly migration away from injection wells (particularly for distances  
48 shorter than 5 km), whereas at larger distances we observe migration toward the wells.

49

50

## 51 1 Introduction

52 In the last decade, seismic activity observed in Oklahoma has attracted considerable public  
53 attention because the annual rate of earthquakes increased since 2009 due to wastewater injection  
54 (Ellsworth, 2013; Weingarten et al., 2015; Hincks et al., 2018). Exploring spatio-temporal  
55 relations between injection wells and seismic migration patterns is key to understanding the  
56 processes controlling the growth of injection-induced seismicity. Earthquakes tend to migrate  
57 away from the fluid source following the diffusion of pore pressure, from which hydraulic  
58 diffusivity properties can be modeled (Shapiro et al., 2005). However, plausible lateral migration  
59 patterns toward or away from injection wells in large-scale fluid-injection stimulated areas such  
60 as Oklahoma remain unclear (Haffener et al., 2018). Yet, if lateral migration patterns exist and  
61 can be tied to (controllable) injection processes, important implications for (time-dependent)  
62 fluid-induced seismic hazard assessment arise. This study investigates such properties through a  
63 comprehensive migration analysis with respect to multiple injection wells for the Oklahoma  
64 seismic clusters. These clusters are defined by applying clustering techniques that associate  
65 seismic events into specific groups (or clusters) with specific spatiotemporal relationships,  
66 deciphering also different fault structures (Ester et al., 1996; Wang et al., 2013; Zaliapin and  
67 Ben-Zion, 2013; Cheng and Chen, 2018). The identification and characterization of these  
68 clusters has been well studied in natural and tectonic contexts revealing interesting event  
69 migration features such as, for instance, event triggering due to fluid flow (Vidale and Shearer,  
70 2006; Chen et al., 2012; Passarelli et al., 2018).

71 Recent efforts for improving the existing earthquake catalogues for Oklahoma identified  
72 seismicity clusters distributed over the area due to the activation of hundreds of previously  
73 unknown faults (Schoenball and Ellsworth, 2017). Analyzing the spatiotemporal evolution of  
74 these clusters reveals that seismicity tends to initiate at shallower depth and migrates deeper  
75 along faults as the sequence proceeds (Schoenball and Ellsworth, 2017b). Although 40 – 50% of  
76 individual clusters exhibit statistically significant diffusive migration, no clear migration patterns  
77 along-strike are observed (Haffener et al., 2018). On the other hand, preferred rupture

78 propagation direction involving directivity effects have been identified for the largest induced  
79 Oklahoma earthquakes (López-Comino and Cesca, 2018; Lui and Huang, 2019). A common  
80 pattern reflecting rupture propagation toward or away from injection wells is difficult to  
81 establish, also due to the variety in rupture styles. The 2011 Mw 5.7 Prague and 2016 Mw 5.0  
82 Cushing earthquakes ruptured away from the injection wells, whereas the 2016 Mw 5.1 Fairview  
83 earthquake ruptured toward the injection. Lui and Huang (2019) attributed the difference in  
84 rupture directions to expected pressurization of the fault zone, which relates to the distance away  
85 from injection zones and total injected volume.

86 Induced seismicity in Oklahoma provides a unique opportunity to systematically compare the  
87 migration direction of each seismic cluster with respect to injection well locations. Each cluster  
88 will be characterized by a so-called migration vector calculated using an enhanced migration  
89 technique based on previous work (Haffener et al., 2018). Seismicity occurs in a region with  
90 many high-rate disposal wells and high-pressure perturbations causing difficulties to establish  
91 appropriate associations among earthquakes and wells. In this context, we introduce a new  
92 methodology to calculate a so-called well vector associated to multiple injection wells. Finally,  
93 we explore plausible lateral migration patterns depending on different parameters such as the  
94 distance from injection wells, injected volumes weightings and equivalent magnitude of each  
95 cluster.

96

## 97 **2 Data**

98 We use a relocated earthquake catalog, recorded between 2010 and 2016, with enhanced spatial  
99 resolution, a magnitude of completeness ( $M_c$ ) of 2.5, and a minimum magnitude of 2.0 (Chen,  
100 2016). We consider individual clusters with at least 20 events identified by Haffener et al.,  
101 (2018). This resulted in 60 clusters after aftershocks were removed using the space-time  
102 windowing method proposed by Uhrhammer (1986) to avoid the space-time imprint of  
103 aftershocks. The injection data used in this study are obtained from Oklahoma Corporation  
104 Commission websites with monthly data from 1995 to 2017 with a total number of 876 disposal  
105 wells. Considering maximum well distances of 50 km, the number of injection wells involved in  
106 this study is 836 (Figure 1).

107

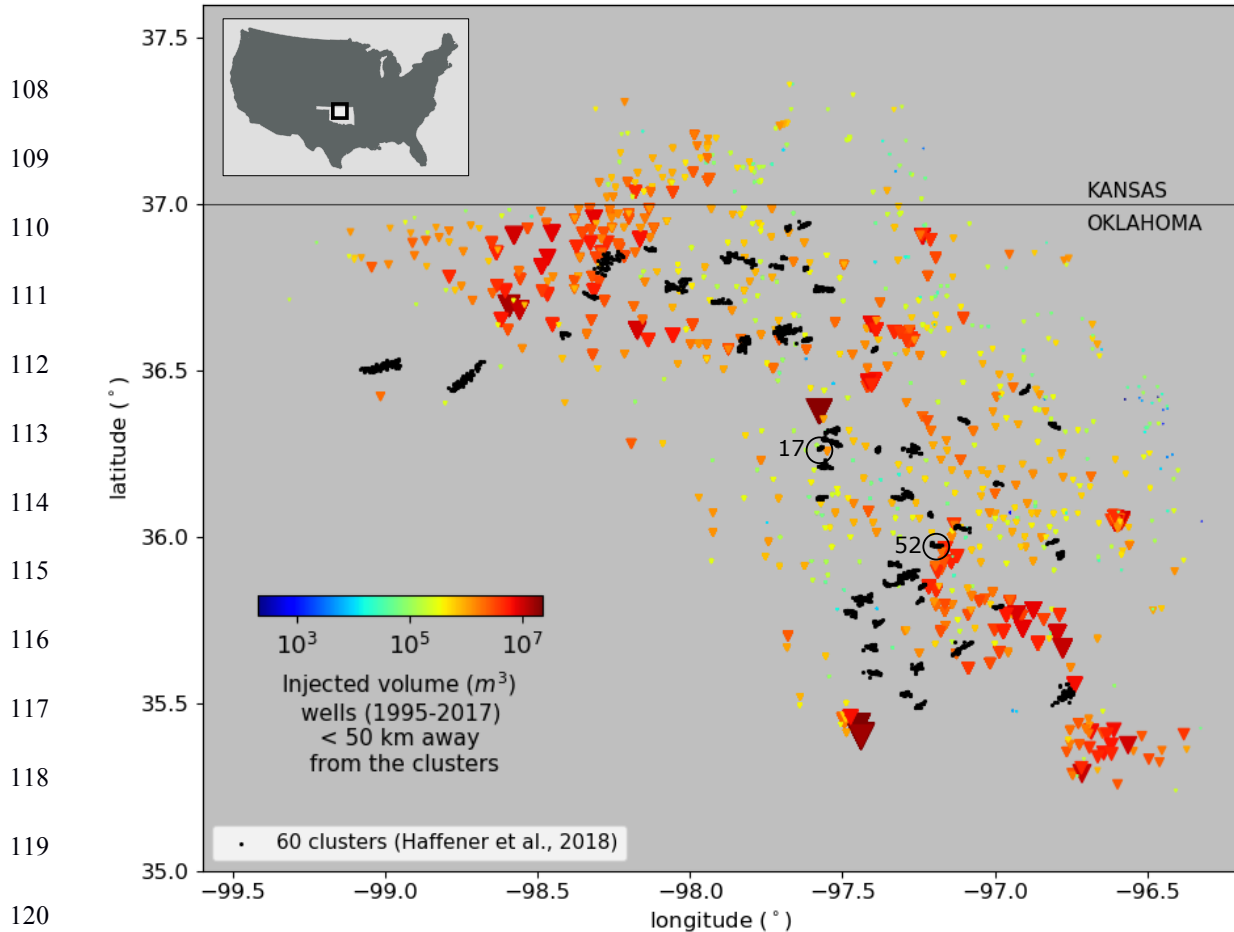


**Figure 1.** Map of wells (inverted triangles) within a radius of 50 km from the average location in each cluster and 60 seismic clusters in Oklahoma (black dots) detected by a nearest-neighbor approach after aftershocks were removed using a space-time windowing method (Haffner et al., 2018). Wells are scaled (color and size) according to the total injected volume between 1995 – 2017. Two selected clusters (17 and 52) analyzed in Figure 2 and S1 are indicated.

### 3 Comprehensive migration analysis with respect to multiple injection wells

In our study, we propose a comprehensive migration analysis based on previous approaches involving different numbers of temporal bins of equal duration spanning the period of the entire sequence (Haffner et al., 2018) (Figure 2 and S1). Earthquakes in each cluster are divided into 10 temporal bins (Figure 2a). A spatial bin point is calculated by averaging epicentral locations in each bin, delineating the migration line of each cluster (Figure 2b).

Next, we define the migration vector ( $\vec{v}_m$ ), as the direction from the 1<sup>st</sup> spatial bin point to the averaged location of the remaining spatial bin points. Each cluster is then characterized by the azimuth  $\Phi$  and length  $r$  of the migration vector (Figure S2). The notation  $\Phi_0$  and  $r_0$  indicates that all events in each cluster were used to calculate the azimuth and length (Figure 2b). To assess uncertainties associated with the calculation of the migration vector, we applied a bootstrap analysis. For each cluster, we calculated 100 migration vectors, randomly removing 10% of events in each repetition (Figure S3). The final  $\Phi$  and  $r$  are then defined from the average

locations of the heads and tails of all migration vectors (Figure 2c). We define the associated uncertainties as  $\varepsilon_\phi = \Delta\Phi/2$ , where  $\Delta\Phi$  is the maximum difference of azimuths calculated from the bootstrap analysis, and  $\varepsilon_r$  as the standard deviation of  $r$ . Significant changes of  $\Phi$  between repetitions indicate that the cluster does not have a prevailing direction of migration (Figure S1). Therefore, we only consider clusters with  $\Delta\Phi < 45^\circ$  in further analysis. Based on this criterion, the migration vectors for 24 clusters were excluded (Figure S4).

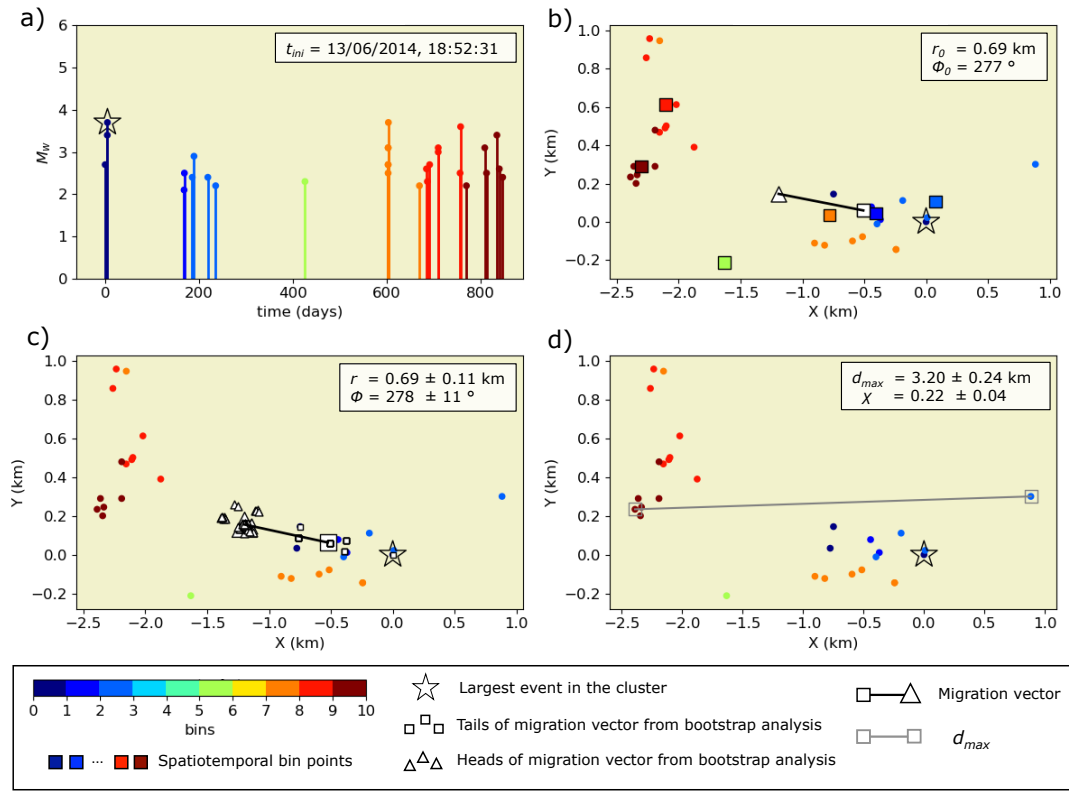


**Figure 2.** Migration analysis for cluster 52 (see Figure 1) showing results for a stable migration vector. a) Temporal evolution of the seismic sequence from  $t_{ini}$ ; the color scale indicates association of seismic events with temporal bins and the star depicts the largest event in the cluster. b) The migration vector (black line) defined from tail (white square) to head (white triangle) and the spatiotemporal evolution of migration (color-coded squares indicate the spatiotemporal bin points).  $r_0$  and  $\Phi_0$  represent the length and azimuth of the migration vector calculated using all events in the cluster. c) Bootstrap analysis to calculate the final length  $r$  and azimuth  $\Phi$  of the migration vector and their uncertainties. Small white triangles and small white squares depict the heads and tails of 100 migration vectors for the bootstrap analysis. The final migration vector is depicted by a black line from the tail (large white square) to the head (large white triangle). d) The maximum cluster length ( $d_{max}$ ) and the migration coefficient ( $\chi$ ) are shown with the uncertainties obtained from the bootstrap analysis.  $d_{max}$  (gray line), is defined by the two seismic events farthest from each other (open gray squares).

Individual clusters are divided into two groups, according to their spatial migration behavior: migration and non-migration groups, or here so-called strong or weak migration groups. Some

176 authors obtain a statistical significance ( $s_m$ ) ranging from 0.5 to 1.0 to identify each migration  
 177 group according a fixed threshold value around 0.8 – 0.85 (Chen et al., 2012). Using such  
 178 criteria, Oklahoma clusters reveal almost a parity division with around 40 – 50 % clusters  
 179 belonging to group with strong migration (Haffener et al., 2018). We propose a simple way to  
 180 quantify this property by calculating the ratio of the length of the migration vector ( $r$ ) to the  
 181 maximum length of the cluster ( $d_{max}$ ) (Figure 2d):

182

183 
$$\chi = \frac{r}{d_{max}} \quad (\text{Eq.1})$$

184

185 The migration coefficient ( $\chi$ ) increases from 0 (no migration) to 1 (strong migration), reaching  
 186 the maximum value only in the case of migration from one end of the cluster to the other.  
 187 Uncertainties for  $\chi$ -values are calculated using the bootstrap analysis. A similar distribution for  $\chi$   
 188 is obtained using different bins to calculate the migration vector where a value of 0.2 yields  
 189 similar results as using  $s_m$  to establish the separation among different migration groups (Figure  
 190 S5).

191 The association of seismic clusters to specific wells is crucial for determining whether clusters  
 192 migrate toward or away from the fluid-injection point. Multiple injection points and the long  
 193 history of injection volumes in Oklahoma complicate the individual associations for each cluster.  
 194 Similar areas in Alberta (Canada) had addressed this issue through spatiotemporal association  
 195 filters, discarding wells potentially not associated with earthquake clusters based on a set of  
 196 association criteria, for instance, epicenters of all temporally associated earthquakes must be  
 197 within 5 km of the well pad surface location (Schultz et al., 2018).

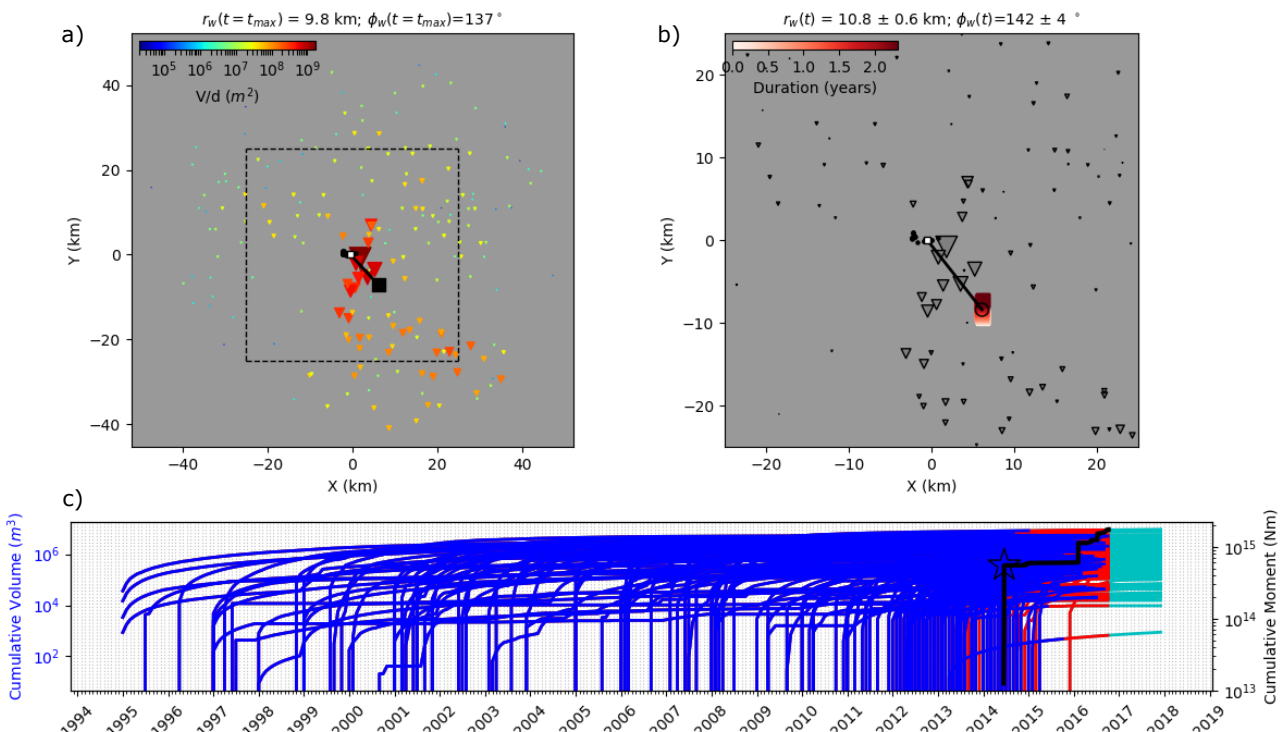
198 Here, we propose a new methodology representing multiple injection wells around each cluster  
 199 using a well vector ( $\vec{v}_w$ ) defined as the vector from the 1<sup>st</sup> spatial bin point of the cluster (used  
 200 previously to define the migration vector) to an injection midpoint (Figure 3). The well vector is  
 201 also characterized by the azimuth  $\Phi_w$  and length  $r_w$  (Figure S2). The injection midpoint is  
 202 determined as the weighted centroid of locations of wells, taking into account the spatial and  
 203 temporal distribution of the volume of injected fluids into individual wells and the expansion of  
 204 the diffusion front. Injected fluids can be associated with a cluster only if they have sufficient  
 205 time to reach the location of the cluster. Considering a linear diffusion model, we approximate  
 206 this time by the diffusion front (Shapiro et al., 2005)

207 
$$t_D = \frac{d^2}{4\pi D}, \quad (\text{Eq.2})$$

208 where  $D$  is diffusion coefficient and  $d$  is the distance between the well and cluster. For the  
 209 analysis, we use a representative value for the diffusion coefficient for Oklahoma area ( $D = 1.5$   
 210  $\text{m}^2/\text{s}$ , Haffener et al., 2018). This corresponds, for example, to a delay time  $t_D$  for the diffusion  
 211 front of about 18 months for a well that is located at 30 km from a cluster (Figure S6). To  
 212 account for the effects of diffusion, a well is associated with a cluster only if the fluid-injection  
 213 started more than  $t_D$  ago. Next, at each time instant  $t$  of the seismic sequence, the weight of an  
 214 individual well  $j$  is adjusted according to reported cumulative injected volume  $V_j(t-t_D)$  and the  
 215 injection rate volume  $\Delta V_j(t-t_D)$ . Note that we consider  $\Delta V$  as the volume injected each month and

216 therefore  $t$  increases in steps of 30 days, consistently with the reporting period of injected  
 217 volumes. Finally, the individual weights are adjusted to account for the expansion of the  
 218 diffusion front such as a geometrical spreading effect. Assuming dominantly horizontal  
 219 diffusion, we consider 2D geometrical spreading, which leads to the weights in the forms of  $V_j(t-t_D)/d_j$   
 220 and  $\Delta V_j(t-t_D)/d_j$ . To avoid singularities, we consider  $d = 1 \text{ km}$  for wells with  $d < 1 \text{ km}$ .

221 Following this procedure, we obtain one injection midpoint for each considered time instant  $t$   
 222 and their average location then defines the final injection midpoint based on weights from  
 223 cumulative injected volume and injection rate volumes, respectively. The procedure for cluster  
 224 52 is illustrated in Figure 3 for cumulative injected volume and in Fig. S7 for injection rate  
 225 volumes. We also define the associated uncertainties as  $\varepsilon_{\phi_w} = \Delta\Phi_w/2$ , where  $\Delta\Phi_w$  is the  
 226 maximum difference of azimuths of individual well vectors, and  $\varepsilon_{rw}$  is the standard deviation of  
 227  $r_w$ . Like for the migration vector, also here cases with  $\Delta\Phi_w > 45^\circ$  are considered unstable. Using  
 228 this criterion, we found 36 stable cases when using the cumulative injected-volume weighting  
 229 and 22 when using the injection-rate volume weighting (Figure S4). A summary of all calculated  
 230 parameters is shown in the Table S1.



243 **Figure 3.** Calculating the well vector for cluster 52 considering the cumulative injected volume  
 244 weighting. a) Situation at the final time of the seismic sequence  $t_{max}$ . The well vector (black line)  
 245 is defined from the tail of the migration vector (white square defined in Fig 2c) to the injection  
 246 midpoint (black square). Length ( $r_w$ ) and azimuth ( $\Phi_w$ ) of the well vector are indicated in the  
 247 figure header. Wells (inverted triangles) are scaled (color and size) according  $V(t_{max}-t_D)/d$ . b)  
 248 Location of injection midpoints during the seismic sequence (color-coded squares). The final  
 249 injection midpoint is shown with an open black circle, the final well vector by the black line.

250 Wells are scaled in size as in a). Only the dashed rectangle from a) is shown. c) Cumulative  
 251 injected volume for the wells associated with the cluster (blue lines) and cumulative seismic  
 252 moment for the seismic sequence (black line; the largest event is indicated by the star). Red lines  
 253 indicate the volume that did not affect the cluster due to diffusion constraints, cyan lines indicate  
 254 data available after the end of seismic sequence.

255

## 256 4 Results

257 To summarize our results of the comprehensive migration analysis considering multiple injection  
 258 wells, we define the direction toward or away from injection wells by a parameter  $\kappa$  that  
 259 represents the angle between the migration vector and the well vector:

$$260 \quad \kappa = \angle(\vec{v}_m, \vec{v}_w). \quad (\text{Eq. 3})$$

261  $\kappa$ -values range from  $0^\circ$  to  $180^\circ$ , with  $\kappa$ -values closer to  $0^\circ$  indicating an alignment among the  
 262 migration vector and the well vector for a migration direction toward the injection wells.  $\kappa$ -  
 263 values closer to  $180^\circ$  indicate the opposite behavior, i.e., migration away from injection wells.  
 264 We note that the migration vector is also affected by fault geometry as it is most likely oriented  
 265 along the fault strike. For this reason, we define  $\kappa < 60^\circ$  as migration toward wells and  $\kappa > 120^\circ$   
 266 as migration away. For intermediate cases ( $60^\circ < \kappa < 120^\circ$ ) the migration and well vectors are  
 267 close to perpendicular, making these cluster a less appropriate choice to decide whether  
 268 seismicity migrates toward or away from the wells.

269 In Figure 4 we compare  $\kappa$  as a function of: i) length of the well vector, ii) the total weights  
 270 assigned to the multiple associated wells based on cumulative injected volumes and injection rate  
 271 volumes, and iii) the equivalent magnitude (sum of the seismic moments of the events in a  
 272 cluster expressed as moment magnitude following Hanks and Kanamori, 1979). For this  
 273 comparison and following analysis, we only consider clusters with strong migration ( $\chi > 0.2$ ): 25  
 274 of 36 clusters for the cumulative volume weighting (Figure 4a) and 14 of 22 clusters for the  
 275 injection rate volume weighting (Figure 4b). Average values and their errors are calculated for  
 276 clusters migrating toward and away from the wells in order to identify potential lateral migration  
 277 patterns. Depending on  $r_w$ , larger differences among these average toward (13 and 16 km) or  
 278 away (8 and 10 km) values are observed for both weightings. However, no significant changes  
 279 are appreciated depending on the weighted volumes and the equivalent magnitude. Additionally,  
 280 the histograms of  $\kappa$ -values for cumulative injected-volume weighting indicate that a small  
 281 majority of clusters (60%) documents a migration away from the wells (Fig 4a4).

282

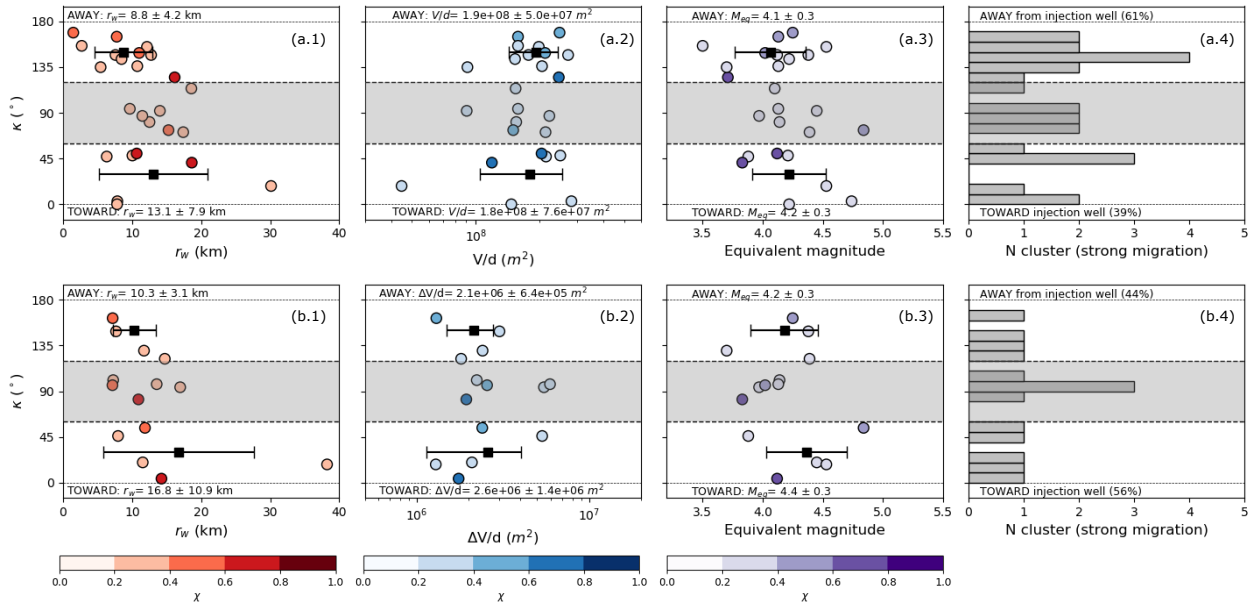


**Figure 4.** Lateral migration patterns toward or away from injection wells characterized by  $\kappa$ -values using 10 temporal bins in the comprehensive migration analysis (for diffusion coefficient of  $1.5 \text{ m}^2/\text{s}$ ).  $\kappa$ -values for strong migration clusters ( $\chi > 0.2$ ) are plotted as circles scaled in color according the migration coefficient ( $\chi$ ), considering the cumulative volume weighting (a) and the injection rate volume weighting (b). Results are shown for each cluster according to the length of the well vector (a.1 and b.1), the total weights assigned to the multiple associated wells in relation to cumulative injected volumes and injection rate volumes (a.2 and b.2) and the equivalent magnitude (a.3 and b.3). Average values and error bars (black squares and lines) are indicated for propagation toward ( $\kappa < 60^\circ$ ) and away ( $\kappa > 120^\circ$ ) from the injection point (see labels). Histograms are also shown including percentages values (a.4 and b.4). Intermediate cases ( $60^\circ < \kappa < 120^\circ$ ) are not considered (gray background separated by black dashed lines).

## 5 Discussion and conclusions

A comprehensive migration analysis is applied to decipher the potential relationship between direction of lateral earthquake migration of induced seismic events and the location of multiple injection wells. We introduced a new parameter,  $\kappa$ , to quantify the direction of lateral migration toward or away from the injection point based on the angle between the migration vector and the well vector. This parameter facilitates the identification of these lateral migration patterns and it can be used to compare results in other fluid-injection stimulated areas.

A representative migration line, obtained by joining spatiotemporal bin points identified for a cluster, yields complex shapes/patterns for clusters with no predominant migration direction or with bilateral migration. To compare results for a large number of clusters, we approximate the trajectory by the migration vector. The migration starting point (generally assumed to be the epicenter of the first recorded seismic event in the cluster) is a relevant parameter to obtain a representative migration vector. However, we consider that the migration starts at the 1<sup>st</sup> spatial bin point, which more accurately defines the first activated fault area than the location of just the

318 single seismic event. Because the complete spatiotemporal history of the seismic sequence must  
319 contribute to defining the head of the migration vector, the average epicentral location of the  
320 remaining spatial bin points is used.

321 We introduced a simple way to quantify the strong/weak migration through a migration  
322 coefficient  $\chi$ , computed from the length of the migration vector and the total length of the  
323 cluster.  $\chi$ -values for all clusters show an asymmetric (positively skewed) distribution with a long  
324 tail toward the largest  $\chi$ -values (Figure S5). A median value of this distribution ( $\chi \sim 0.2$ )  
325 provides similar results as using  $s_m$  criterions to divide the Oklahoma clusters into strong/weak  
326 migration groups. Clusters with  $\chi$ -values larger than 0.2 show an observable migration, but  
327 below this value the length of the migration vector is too short to observe any predominant  
328 migration directions.

329 We also propose a new strategy to define representative well vectors associated with multiple  
330 injection points surrounding a seismic cluster, considering two types of weighting. The  
331 cumulative volume weighting may better represent cumulative effects of pore pressure build up  
332 from the beginning of the injection, while injection rate volume weighting may better represent  
333 effect of pore pressure variations. From an operational point of view, injection rate weighting  
334 may vary significantly over a short time scale, which can cause significant changes of the  
335 direction of the well vector during the course of the cluster (Figure S7), as documented by 22  
336 identified unstable well vectors. In contrast, the cumulative volume weighting provides more  
337 stable results with no unstable well vectors (Figure S4). Also, different directions of the well  
338 vector can be found for each weighting in the same cluster (Fig 3b and S7b).

339 Regardless of the influence of the weighting on well vector orientation, we observe similar  
340 patterns when comparing propagation towards (small  $\kappa$ ) and away (large  $\kappa$ ) from the wells,  
341 depending on the  $r_w$  (Figure 4a.1 and 4b.1) and the equivalent magnitude (Figure 4a.3 and 4b.3).  
342 Significant differences are observed only according to  $r_w$ , revealing the cluster-well distances as  
343 a key factor to control these processes. Migration away from injection wells is found for  
344 distances shorter than 5-13 km, while an opposite migration towards the wells is observed for  
345 larger distances. Both distributions overlap, indicating that there is no moncausal relationship  
346 with distance, but the general trend is clear. Accordingly, at shorter cluster-well distances where  
347 hydraulic connections between faults and injection wells can be involved, the seismicity is  
348 triggered by propagating pore-pressure front (Shapiro et al., 2005). The cumulative injected  
349 volume weighting provides the most stable results revealing clearly this pattern for cluster with  
350  $r_w < 5$  km. For larger distances, the previous assumption becomes questionable. Outside of the  
351 high-pressure zone, poroelastically-induced Coulomb-stress-changes should surpass pore  
352 pressure changes, providing a plausible triggering mechanism in the far-field of injection wells  
353 (Goebel et al., 2017). The transition from pore-pressure dominance to poroelastic stress based on  
354 distance could explain the changes in migration pattern at further distances, which is observed  
355 for  $r_w$  in the range between 5 - 20 km. For  $r_w > 20$  km, our only observation corresponds to the  
356 Woodward cluster, confirming this behavior.

357 The observed patterns remain stable for different choices of the diffusion coefficient ( $D = 1.25 -$   
358  $1.75 \text{ m}^2/\text{s}$ , Fig S8 and S9), which further supports robustness of the well vector-based approach.  
359 Also, different choices of temporal binning (5, 10, 15 and 20) yield similar and consistent results  
360 (Figs S10 and S11). Considering only 2 bins in the injection rate volume weighting, we obtain

similar results such as the statistical parameter  $d_s$  which assesses the distance separation between the centers of the first half and second half of each cluster (Chen and Shearer, 2011; Chen et al., 2012). Overall, the comparison indicates that 10 bins is a reasonable choice for our study.

Folesky et al. (2016) analyzed the directivity effects of the largest seismic events associated with the stimulation of geothermal reservoir in Basel (Switzerland) and found that the preferred rupture propagation depends on magnitude. They found that events with  $M_L > \sim 2$  propagated backward into the perturbed volume while smaller events propagated away from the well. Our analysis, with minimum equivalent magnitudes around 3.5, shows a different situation, with a significant number of clusters migrating away from the injection wells, and no clear dependence on magnitude.

In conclusion, albeit the main migration pattern in Oklahoma reflects a downward migration from the Arbuckle layer to the basement (Schoenball and Ellsworth, 2017b, Haffener et al., 2018), we found clear lateral migration patterns involving the cluster-well distance as the main factor to control preferred migration directions toward or away from the injection wells. While clusters closest to the wells show a predominant migration away from the wells attributed to pore-pressure changes, we also observe an opposite behavior toward the wells for larger distances that could be controlled by poroelastic stress changes.

378

### 379 Acknowledgments

We thank the Oklahoma Geological Survey (OGS) and USGS for continuous monitoring earthquake activities in Oklahoma. The catalogs for earthquake are obtained from OGS (<https://www.ou.edu/ogs>) and the seismic clusters from Haffener et al., 2018. The disposal well data are obtained from Oklahoma Corporation Commission (OCC). The research presented in this article is supported by King Abdullah University of Science and Technology (KAUST) in Thuwal, Saudi Arabia, by FRAGEN project (Fracture activation in geo-reservoirs - physics of (induced) earthquakes in complex fault networks), URF/1/3389-01-01, BAS/1/1339-01-01, and Spanish project CGL2015-67130-C2-2-R. J.A.L.C has also received funding from the European Union's Horizon 2020 research and innovation programme under the Marie Skłodowska-Curie grant agreement N° 754446 and UGR Research and Knowledge Transfer Found – Athenea3i; and by the Deutsche Forschungsgemeinschaft (DFG, German Research Foundation) – Projektnummer (407141557). We also thank Justin Rubinstein and Simone Cesca for constructive comments and discussions. We thank two anonymous reviewers and the GRL Associate Editor for invaluable comments that helped to improve this study.

394

395 **References**

- 396
- 397 Chen, C. (2016). Comprehensive analysis of Oklahoma earthquakes: From earthquake  
398 monitoring to 3D tomography and relocation (Phd dissertation), University of Oklahoma.
- 399 Chen, X., Shearer, P. M., & Abercrombie, R. (2012). Spatial migration of earthquakes within  
400 seismic clusters in Southern California: Evidence for fluid diffusion. *Journal of*  
401 *Geophysical Research*, 117, B04301. <https://doi.org/10.1029/2011JB008973>
- 402 Cheng, Y., & Chen, X. (2018). Characteristics of seismicity inside and outside the Salton Sea  
403 Geothermal Field. *Bulletin of the Seismological Society of America*, 108, 1877–1888.  
404 <https://doi.org/10.1785/0120170311>
- 405 Ellsworth, W. L. (2013). Injection-induced earthquakes. *Science*, 341, no. 6142, 1–7.
- 406 Ester, M., Kriegel, H.-P., Sander, J., & Xu, X. (1996). A density-based algorithm for discovering  
407 clusters in large spatial databases with noise. In *Proceedings of the 2nd International*  
408 *Conference on Knowledge Discovery and Data Mining* (KDD-96). Portland, OR: AAAI  
409 Press.
- 410 Goebel, T., Weingarten, M., Chen, X., Haffner, J., & Brodsky, E. E. (2017). The 2016 Mw 5.1  
411 Fairview, Oklahoma earthquakes: Evidence for long-range poroelastic triggering at >40  
412 km from fluid disposal wells. *Earth and Planetary Science Letters*, 472, 50–61.  
413 <https://doi.org/10.1016/j.epsl.2017.05.011>
- 414 Folesky, J., J. Kummerow, S. A. Shapiro, M. Häring, and H. Asanuma (2016). Rupture  
415 directivity of fluid-induced microseismic events: Observations from an enhanced  
416 geothermal system, *J. Geophys. Res.* 121, no. 11, 8034–8047.
- 417 Haffner, J., Chen, X., & Murray, K. (2018). Multiscale analysis of spatiotemporal relationship  
418 between injection and seismicity in Oklahoma. *Journal of Geophysical Research: Solid*  
419 *Earth*, 123. <https://doi.org/10.1029/2018JB015512>
- 420 Hanks, T., and H. Kanamori (1979), A moment magnitude scale, *J. Geophys. Res.*, 84, 2348–  
421 2350.
- 422 Hincks, T. , Aspinall, W. , Cooke, R. and Gernon, T. (2018). Oklahoma's induced seismicity  
423 strongly linked to wastewater injection depth, *Science* 359 (6381), 1251-1255.
- 424 Lopez-Comino, J. A., & Cesca, S. (2018). Source complexity of an injection induced event: The  
425 2016 Mw 5.1 Fairview, Oklahoma earthquake. *Geophysical Research Letters*, 45, 4025–  
426 4032. <https://doi.org/10.1029/2018GL077631>
- 427 Lui, S. K. & Huang, Y. (2019). Do injection-induced earthquakes rupture away from injection  
428 wells due to fluid pressure change? *Bulletin of the Seismological Society of America*,  
429 109(1), 358-371.
- 430 Passarelli, L., Rivalta, E., Jónsson, S., Hensch, M., Metzger, S., Jakobsdóttir, S. S., Maccaferri,  
431 F., Corbi, F., Dahm, T. (2018): Scaling and spatial complementarity of tectonic  
432 earthquake swarms. - *Earth and Planetary Science Letters*, 482, pp. 62-70. DOI:  
433 <http://doi.org/10.1016/j.epsl.2017.10.052>

- 434 Schoenball, M., & Ellsworth, W. L. (2017). Waveform relocated earthquake catalog for  
435 Oklahoma and Southern Kansas illuminates the Regional Fault Network. *Seismological*  
436 *Research Letters*, 88(5), 1252–1258. <https://doi.org/10.1785/0220170083>
- 437 Schoenball, M., & Ellsworth, W. L. (2017b). A systematic assessment of the spatiotemporal  
438 evolution of fault activation through induced seismicity in Oklahoma and southern  
439 Kansas. *Journal of Geophysical Research: Solid Earth*, 122, 10,189–10,206.
- 440 Schultz, R., Atkinson, G., Eaton, D. W., Gu, Y. J. & Kao, H. (2018). Hydraulic fracturing  
441 volume is associated with induced earthquake productivity in the Duvernay play, *Science*  
442 359, 6373, 304–308, doi: 10.1126/science.aa0159.
- 443 Shapiro, S. A., Rentsch, S., & Rothert, E. (2005). Characterization of hydraulic properties of  
444 rocks using probability of fluid-induced microearthquakes. *Geophysics*, 70(2), F27–F33.  
445 <https://doi.org/10.1190/1.1897030>
- 446 Uhrhammer, R. (1986). Characteristics of northern and southern California seismicity.  
447 *Earthquake Notes*, 57(1), 21.
- 448 Vidale, J. E., and P. M. Shearer (2006), A survey of 71 earthquake bursts across southern  
449 California: Exploring the role of pore fluid pressure fluctuations and aseismic slip as  
450 drivers, *J. Geophys. Res.*, 111, B05312, doi:10.1029/2005JB004034.
- 451 Wang, Y., G. Ouillon, J. Woessner, D. Sornette, S. Husen (2013). Automatic reconstruction of  
452 fault networks from seismicity catalogs including location uncertainty, *Journal of*  
453 *Geophysical Research: Solid Earth* 118 (11), 5956-5975, doi: 10.1002/2013JB010164,
- 454 Weingarten, M., Ge, S., Godt, J., Bekins, B., & Rubinstein, J. (2015). High-rate injection is  
455 associated with the increase in U.S. mid-continent seismicity. *Science*, 348(6241), 1336–  
456 1340. <https://doi.org/10.1126/science.aab1345>
- 457 Zaliapin, I., & Ben-Zion, Y. (2013). Earthquake clusters in southern California I: Identification  
458 and stability. *Journal of Geophysical Research: Solid Earth*, 118, 2847–2864.  
459 <https://doi.org/10.1002/jgrb.50179>